Spin-wave localization on phasonic defects in a one-dimensional magnonic quasicrystal

Szymon Mieszczak,* Maciej Krawczyk, and Jarosław W. Kłos
Institute of Spintronics and Quantum Information, Faculty of Physics, Adam Mickiewicz University, Poznań, Uniwersytetu Poznańskiego 2, Poznań 61-614, Poland

(Received 5 May 2022; accepted 16 August 2022; published 25 August 2022)

We report on the evolution of the spin-wave spectrum under structural disorder introduced intentionally into a one-dimensional magnonic quasicrystal. We study theoretically a system composed of ferromagnetic strips arranged in a Fibonacci sequence. We considered several stages of disorder in the form of phasonic defects, where different rearrangements of strips are introduced. By transition from the quasiperiodic order towards disorder, we show a gradual degradation of spin-wave fractal spectra and closing of the frequency gaps. In particular, the phasonic defects lead to the disappearance of the van Hove singularities at the frequency gap edges by moving modes into the frequency gaps and creating new modes inside the frequency gaps. These modes disperse and eventually can close the gap, with increasing disorder levels. The work reveals how the presence of disorder modifies the intrinsic spin-wave localization existing in undefected magnonic quasicrystals. The paper contributes to the knowledge of magnonic Fibonacci quasicrystals and opens the way to study of the phasonic defects in two-dimensional magnonic quasicrystals.

DOI: 10.1103/PhysRevB.106.064430

I. INTRODUCTION

Quasicrystals are aperiodic structures characterized by long-range order and lack of translational symmetry [1,2]. The order can be revealed in the Fourier spectrum of the structure that has a countable set of Fourier components [3–6]. This property leads to the presence of multiple frequency gaps (i.e., Bragg gaps) in the spectrum of eigenmodes. The disorder introduced into the structure generally leads to the localization of the eigenmodes. The increasing level of disorder eventually leads to Anderson localization [7–10] and the gradual closing of the Bragg gaps. Particularly interesting is the case of defects in quasicrystals because they possess fine band structures and already localized modes that are called critically localized. In this sense, the impact of the disorder can be more complex.

Due to the structural degrees of freedom in quasicrystals, the local arrangement of the structure cannot unambiguously determine the global ordering and the identification of disorder is more difficult than for periodic structures. The concept of structural degrees of freedom is more understandable when we notice that the quasicrystals can be generated from the higher-dimensional crystals defined in abstract higher-dimensional hyperspace or real space but by the cut-and-projection (C&P) method [3].

The most known one-dimensional (1D) quasicrystal whose lattice can be generated by the C&P method is the Fibonacci quasicrystal, where lattice points, separated by long ($L = a\tau/\sqrt{2+\tau}$) and short ($S = a/\sqrt{2+\tau}$) distances, are arranged aperiodically (a denotes the period of square lattice in hyperspace, τ is the golden ratio) [11]. The translation of the Fibonacci lattice is equivalent to rearrangements/swaps within the pairs of neighboring sites, which leads to the exchange of the adjacent short and long distances: $LS \leftrightarrow SL$. These local rearrangements of the lattice are called *phasons* [12]. The C&P method suggests also how to generate the positional disorder in the Fibonacci lattice manifested only by the perturbation of the sequence of L and S. It can be achieved by the modulation of the shift c of the projection line $y = \tau^{-1}x + c(x)$—see Appendix A for more details. If this randomly introduced modulation is long wave and has small amplitude, then it generates the $LS \leftrightarrow SL$ swaps. Such kind of structural disorder is called *phasonic defects*.

The phasons (and phasonic defects) are the unique feature of all quasicrystals and were intensively investigated in relation to the stability of the atomic lattice of natural quasicrystals and their phononic properties [13]. In these systems, phasons are dynamic objects which can be activated thermally and move diffusely [10,14,15] in the structure of a quasicrystal. The concept of phasons was already investigated in photonics including the diffusive character of phasons [16]. Their role was also discussed as static defects, deliberately introduced into the photonic quasicrystals [17].

In the paper we focus on the general problem of proper introduction of positional disorder in magnonic quasicrystals and study the impact of such phasonic defects on the spin-wave spectra and their localization properties in magnonic Fibonacci quasicrystals [18,19]. We introduce the static and spatially uncorrelated phasonic defects, which allow for gradual transition from the nondefected Fibonacci sequence of strips to the completely disordered system. The static character of considered phasonic defects means that they are introduced intentionally (i.e., by design) and not spontaneously (i.e., by thermal activation).

The impact of the disorder on magnetization dynamics was extensively studied in the lattice models [20–23]. In the case of the continuous model, the impact of the isolated

*szymon.mieszczak@amu.edu.pl

defect on the spin-wave spectrum in magnonic crystals was investigated for 1D structures [24–26], two-dimensional (2D) magnonic crystals [27–29], and line defects in 2D magnonic crystals [30]. There were also reports on defect as a magnetization reversal of a single strip in a one-dimensional magnonic crystal [31]. However, a disorder in magnonic quasicrystals raises another class of questions, thus, we believe that our study on phasonic defects and their impact on the spin waves makes a valuable contribution to the magnonics field of research.

In Sec. II we present the magnonic structure under investigation, explaining (i) why this structure can be considered as a decorated Fibonacci lattice and (ii) how we introduce the uncorrelated phasonic defects. In this section we also outline the computational method based on the solution of the Landau-Lifshitz equation by the plane wave method. In Sec. III we provide a detailed analysis of the impact of the phasonic defect on the frequency spectra of SWs and localization of the modes, illustrated by the plots of the integrated density of states, localization measure, and the profiles of selected modes. Finally, in Sec. IV we conclude our findings.

II. STRUCTURE AND MODEL

We investigate spin waves (SWs) in a 1D planar magnonic structure composed of cobalt (Co) and permalloy (Py) strips of equal widths, being in direct contact and thus forming a continuous layer. The Co and Py strips are magnetically saturated by the external field applied along with them. The strips are arranged in a Fibonacci quasicrystal. It is worth noting that despite the equal width of the strips, the system can be understood as a decorated Fibonacci lattice where Co and Py strips are centered at sequences *SLLS* and *SLS* sharing the shorter sections *S* between Co and Py with the ratio $(2-\tau)/(2+\tau)$. Then, the common width of Co and Py strips is equal to $a(\frac{3}{2}\tau+1)/\sqrt{\tau+2}$.

To generate the phasonic defects as the structural perturbations, we use the procedure which is technically simpler than the C&P method (discussed in Appendix A), although it is based on a more complex formalism (describing the properties of the generalized Harper model with incommensurate modulation of the on-diagonal and off-diagonal elements of tight-binding Hamiltonian [32]). The general model, which also describes the Fibonacci quasicrystal, is presented in Ref. [32]. The authors provide the characteristic equation that determines the successive elements of the Fibonacci sequence for given values of the parameter ϕ, describing the structural degree of freedom [33,34]:

$$\chi_n(\phi) = \mathrm{sgn}\left[\cos\left(\frac{2\pi n}{\tau}+\phi\right)-\cos\left(\frac{\pi}{\tau}\right)\right]. \qquad (1)$$

The characteristic function χ_n takes the values ± 1. For our structure, $\chi_n = 1$ ($\chi_n = -1$) selects Py (Co) strip at nth position in the Fibonacci sequence. The parameter ϕ is related to the shift c of the line $y = \tau^{-1}x + c$ in the C&P method: $\phi = 2\pi c/a$, see Fig. 9 in Appendix A. For infinite range of the index n, the different values of ϕ correspond to different realizations of the Fibonacci crystals which are only shifted by $\tilde{n}$ positions with respect to each other: $\chi_n(\phi) = \chi_{n+\tilde{n}}(\phi+\tilde{\phi})$, for every n (the change $\tilde{\phi}$ of the parameter ϕ corresponds to the shift of the sequence by $\tilde{n}$ positions). When n takes values in the finite range $1,\ldots,N$, where N is the Fibonacci number, then the sweep of the parameter ϕ in the range $[0, 2\pi]$ produces all unique, N-element sequences which can be identified as the Fibonacci crystal. The number of such unique approximates of the Fibonacci crystal is equal to N. It is illustrated in Fig. 1(a) where we presented all 21 approximates composed of 21 elements (strips). Please note that the characteristic function Eq. (1) is periodic: $\chi_n(\phi) = \chi_n(\phi+2\pi)$, and the parameter ϕ plays a role of phase in Eq. (1).

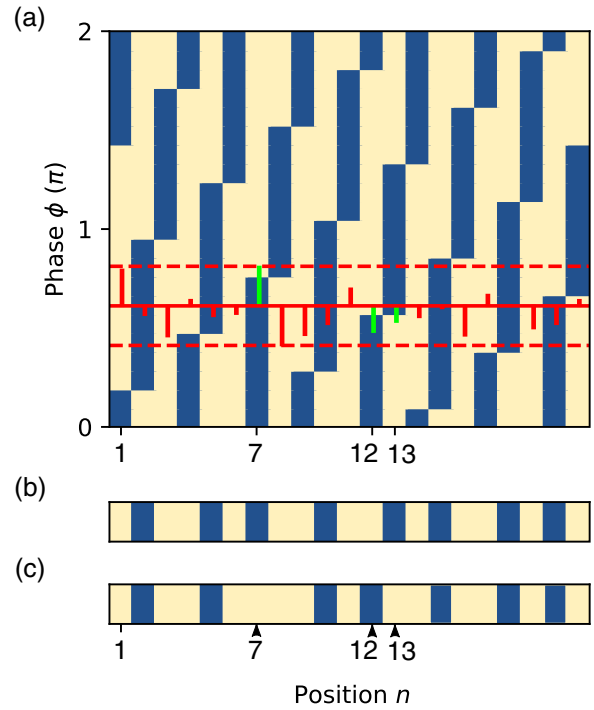

FIG. 1. (a) All possible approximates of a Fibonacci crystal composed of 21 elements. As the phase ϕ changes [see Eq. (1)], we obtain 21 possible sequences of Co (light yellow) and Py (dark blue)—note that Co strips can appear in doublets. The solid red line at $\phi = \pi/\tau$ corresponds to the approximate generated by standard substitution rules: Co $\rightarrow$ Co|Py, Py $\rightarrow$ Co, presented in (b)—see also Fig. 2. The red dashed lines show the range in which the parameter ϕ is randomly changed at each position n. The changes of ϕ which induces the phasonic defects are marked by green bars. They are responsible for the substitution Py $\rightarrow$ Co at position 7 and swap between positions 12 and 13 (Co|Py $\rightarrow$ Py|Co). A sequence with defects is presented in (c); note that position of swaps are marked by arrows.

We arbitrarily selected the structure represented by $\phi = \pi/\tau$ because this approximate is generated by the standard substitution rules. The phasonic defects can be introduced to any sequence generated by Eq. (1), because each of them is a defectless section of the Fibonacci quasicrystal. The approximate for $\phi = \pi/\tau$ [red solid line in Fig. 1(a)] is presented schematically in Fig. 1(b) and a corresponding structure is visualized in Fig. 2.

To introduce the phasonic defects we add an additional term ϕ_n to the parameter ϕ: $\phi \rightarrow \phi + \tilde{\phi} + \phi_n$ [33,34]. This term is a random number of uniform distribution in the range $-\Delta\phi < \phi_n < \Delta\phi$, where $\Delta\phi < \pi$. The range $\Delta\phi$ can be understood as a counterpart of thermodynamic temperature

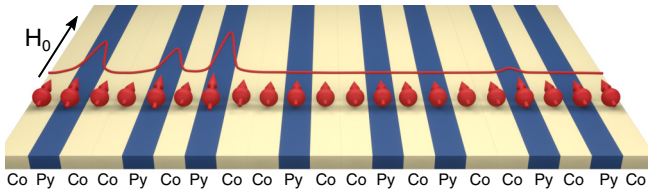

FIG. 2. The approximate of a Fibonacci quasicrystal corresponding to the $\phi = \pi/\tau$ (see Fig. 1), i.e., resulting from the standard substitution rules: Co $\rightarrow$ Co|Py, Py $\rightarrow$ Co. This exemplary structure is composed of Py and Co flat strips (30 nm thick and 300 nm wide), aligned side-by-side and being in direct contact. The field $\mu_0 H_0 = 0.1$ T is applied along the strips. The sequence of tilted arrows and line in front of them visualizes the spin-wave mode profile.

in atomistic quasicrystals, where higher temperature leads to higher probability of defect occurrence. This range is marked by the red dashed lines in Fig. 1(a) and the exemplary sample of the random values of ϕ_n are denoted by thin vertical bars. The perturbations ϕ_n which induce the phasonic defects (i.e., flip the sign of χ_n) are marked by the green line (positions $n = 7, 12, 13$). The ineffective perturbations are marked by red bars. The perturbed structures with three phasonic defects are shown in Fig. 1(c). Positions of phasonic defects are marked by arrows below the figure. The defects are not correlated in space because for each position χ_n is generated independently. Thus, the parameter ϕ_n does not change gradually, in a wavelike manner, as it is expected for a long wave (and long-living) phasons in atomic quasicrystals at finite temperature [13,14]. Because of it, along with swaps $LS \leftrightarrow SL$, we can also observe the substitutions $L \leftrightarrow S$. For $\Delta\phi = \pi$ the system becomes random, since the probability of a type of strip at nth position is τ. We discuss this case in Appendix B. For smaller values of the amplitude $\Delta\phi$, the introduction of defect is not equally probable at every position. At some locations (e.g., position 13 in Fig. 1) the generation of the defect is highly probable, whereas other locations can be quite robust (e.g., position 7), or even completely inaccessible (e.g., position 2) for defects [35].

Each strip is assumed to have a width of 300 nm, a thickness of 30 nm, and is infinitely long. The dimensions make the system in an exchange-dipolar regime, which is already feasible for experimental realization. For the constituent elements from which the system is constructed, we consider two widely used materials, namely Co and Py. The parameters that are important for SW propagation are magnetization saturation M_S and the exchange length λ_{ex}. These parameters are equal to $M_{S,Co} = 1445$ kA/m, $\lambda_{ex,Co} = 4.78$ nm, $M_{S,Py} = 860$ kA/m, and $\lambda_{ex,Py} = 5.29$ nm. We assume that our sample is saturated by the external magnetic field with value $\mu_0 H_0 = 0.1$ T, and is directed along the strips. In this geometry a static demagnetizing field is equal to zero.

We consider a magnonic quasicrystal that is composed of two different magnetic materials [36,37]. However, the magnetic contrast can also be obtained in other ways: By inducing local anisotropy [38,39], by decorating the uniform film [40,41], or by thermal gradient [42]. Having said that, the physics that we present in the paper is not restricted to the bicomponent material.

When we neglect the damping, the dynamics of the magnetization vector can be described by the Landau-Lifshitz equation (LLE):

$$\frac{\partial \boldsymbol{M}}{\partial t} = -\mu_0 |\gamma| \boldsymbol{M} \times \boldsymbol{H}_{\text{eff}}, \tag{2}$$

where $\mu_0 = 4\pi \times 10^{-7}$ H/m is the permeability of vacuum and $\gamma = 176$ rad GHz/T is the gyromagnetic ratio. The effective magnetic field, which contains all kinds of magnetic interactions considered in our study, governs the precession of the magnetization vector. In our case $\boldsymbol{H}_{\text{eff}}$ is composed of the following terms:

$$\boldsymbol{H}_{\text{eff}}(\boldsymbol{r}, t) = \boldsymbol{H}_0 + \boldsymbol{H}_{\text{dm}}(\boldsymbol{r}, t) + \boldsymbol{H}_{\text{ex}}(\boldsymbol{r}, t), \tag{3}$$

where $\boldsymbol{H}_0$ stands for the external field, $\boldsymbol{H}_{\text{dm}}(\boldsymbol{r}, t)$ is the demagnetizing field, and $\boldsymbol{H}_{\text{ex}}(\boldsymbol{r}, t)$ is the exchange field. The last two terms are spatially and temporally dependent since they are connected with material parameters and magnetization dynamics at the same time. SWs are usually studied at room temperatures T. Considered materials have much higher Curie temperatures T_C, e.g., $T_C \approx 1400$ K for cobalt. In the regime $T \lesssim 3/4 T_C$, thermal effects can be neglected, and the usage of the LLE is fully justified [43].

We use the plane wave method (PWM) to solve the linearized LLE [44], where the magnetization vector $\boldsymbol{M}(\boldsymbol{r}, t)$ can be decomposed into static part $M_0(\boldsymbol{r})$ and dynamic $\boldsymbol{m}(\boldsymbol{r}) e^{i2\pi f t}$, changing harmonically with the frequency f. The dynamic part contains two components of magnetization vector: $m_{\text{in}}(\boldsymbol{r}, t)$ and $m_{\text{out}}(\boldsymbol{r}, t)$, representing in-plane and out-of-plane oscillation, respectively. The PWM method is designed for a periodic system, where the Bloch boundary condition must be used. The PWM is based on the application of the Fourier transform both to the Bloch functions (dynamic components of magnetization) and material parameters (saturation magnetization and exchange length). These procedures allow us to formulate an algebraic eigenproblem which can be solved numerically with the eigenvalues (being eigenfrequencies) and eigenvectors (being the Fourier coefficients of the Bloch functions).

Despite the fact that the quasicrystals are not periodic structures, the PWM can still be used in the so-called supercell approach [45]. This application of PWM still assumes periodicity, but for supercells being copies of the whole system, for which we take the periodic boundary condition. In magnonics, this approach was already used to investigate defect modes [24], interface modes [46], waveguides [47], and two-dimensional quasicrystals [48,49]. For the considered system, the supercells are composed of 377 strips. For such large supercells the peculiarities of the Fibonacci quasicrystal are well reproduced, and spurious interface states (which can appear at the edges of supercells) do not disturb the spectra. We used 3770 plane waves for expansion into the Fourier series. This amount was checked for convergence and was enough to reproduce the Fibonacci spectra [19].

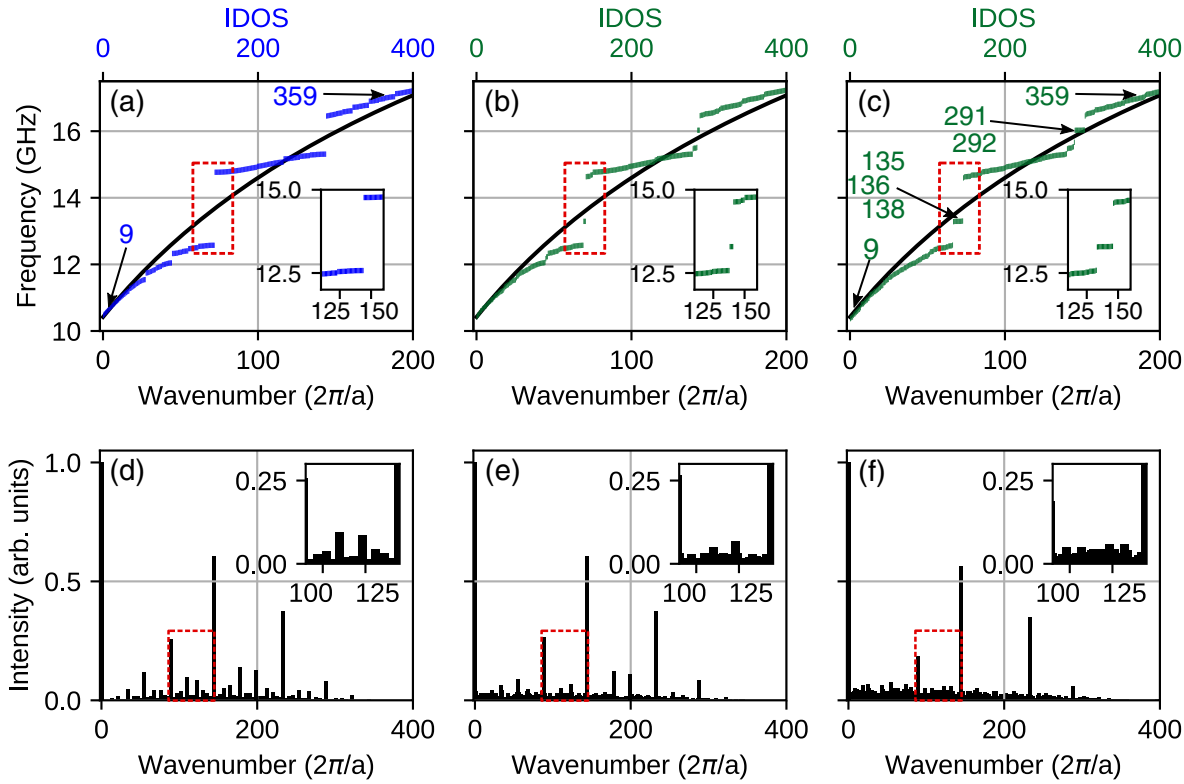

FIG. 3. Top row: (a), (b), and (c) Integrated density of states as a function of frequency plotted in the inverse form f(IDOS) (blue/green color), and the dispersion relation for SWs in a homogeneous film with weight averaged material parameters (black color). Please note that IDOS and dispersion relation has their own abscissa, and shares a common ordinate. The abscissa of each plot has the same scale, indicated only in the leftmost plot. (a) Results obtained for a perfect Fibonacci sequence composed of 377 strips. (b) Results obtained for a defected sequence with amplitude $\Delta\phi/(2\pi) = 5\%$ and (c) $\Delta\phi/(2\pi) = 10\%$. Bottom row: (d), (e), and (f) Bar plot of reciprocal lattice vector intensities, corresponding to the Bragg peaks, for the structures from (a), (b), and (c), respectively. Phasonic defects destroy the fine structure of Bragg peaks that in consequence lead to modification of the density of states at the edges of frequency gaps and creates new modes inside the gaps.

III. RESULTS AND DISCUSSION

To determine the spectral properties of the approximates of the Fibonacci quasicrystal, we plotted the dependence of integrated density of states (IDOS) on the frequency. For a finite system, IDOS(f) is the number of modes below a given frequency f, see Refs. [19,48,50]. For the successive approximates of a 1D crystal or quasicrystal (i.e., taking larger unit cell), the IDOS is a steplike function where the steps become finer with the increasing size of the approximates. Constant frequency ranges in the IDOS(f) corresponds to the frequency gap of the system for $k = 0$. The width of these ranges converges with larger approximates. The other feature allowing the identification of the frequency gaps is a specific character of IDOS(f) close to the gap's edges. The changes of the frequencies for successive modes (i.e., with increasing IDOS) become extremely small in the vicinity of the gap, which is the manifestation of van Hove singularities in the density of states for 1D nondefected systems [51,52]. It is worth noting that, due to the lack of translational symmetry in quasicrystals, we cannot easily relate the frequency f to the wave number k. However, it was shown that for a 1D infinite system, the IDOS(f) $\propto k(f)$ [53]. Therefore, the IDOS(f) dependence for large approximates give us insight into the dispersion relation $f(k)$, see Figs. 3(a)–3(c).

The f(IDOS), i.e., inverse function of IDOS(f), for a nondefected approximate (composed of 377 strips) is presented in Fig. 3(a). The solid black line in Figs. 3(a)–3(c) shows the dispersion relation $f(k)$ for an infinite uniform thin film [54]. Please note the split of the x axis between IDOS and the wave number. The film was assumed to have effective material parameters, which are the volume averages of the constituent material parameters of Co and Py. It is clearly seen that the f(IDOS) follows the dispersion relation $f(k)$. The agreement is very good for long SWs, in the so-called metamaterial regime ($k \to 0$). In this case, SWs are not that sensitive to a specific configuration of strips. Significant differences are observed when frequency gaps are opened, which does not appear in the homogeneous film. Just before and after frequency gaps, differences between the frequencies of successive states are very small, and bars in the graph [Fig. 3(a)] form the horizontal lines, which corresponds to the van Hove singularities.

Figures 3(b) and 3(c) show f(IDOS) in the presence of phasonic defects. We used green color for IDOS to visually differentiate results from the nondefected case in Fig. 3(a). We consider two levels of phasonic defects corresponding to different ranges $\Delta\phi$ of the random component of the parameter ϕ, which describes the structural degree of freedom [see, Eq. (1) and Fig. 1]. We assume the values $\Delta\phi/(2\pi) = 5\%$ [Fig. 3(b)] and 10% [Fig. 3(c)]. Due to phasonic defects, the

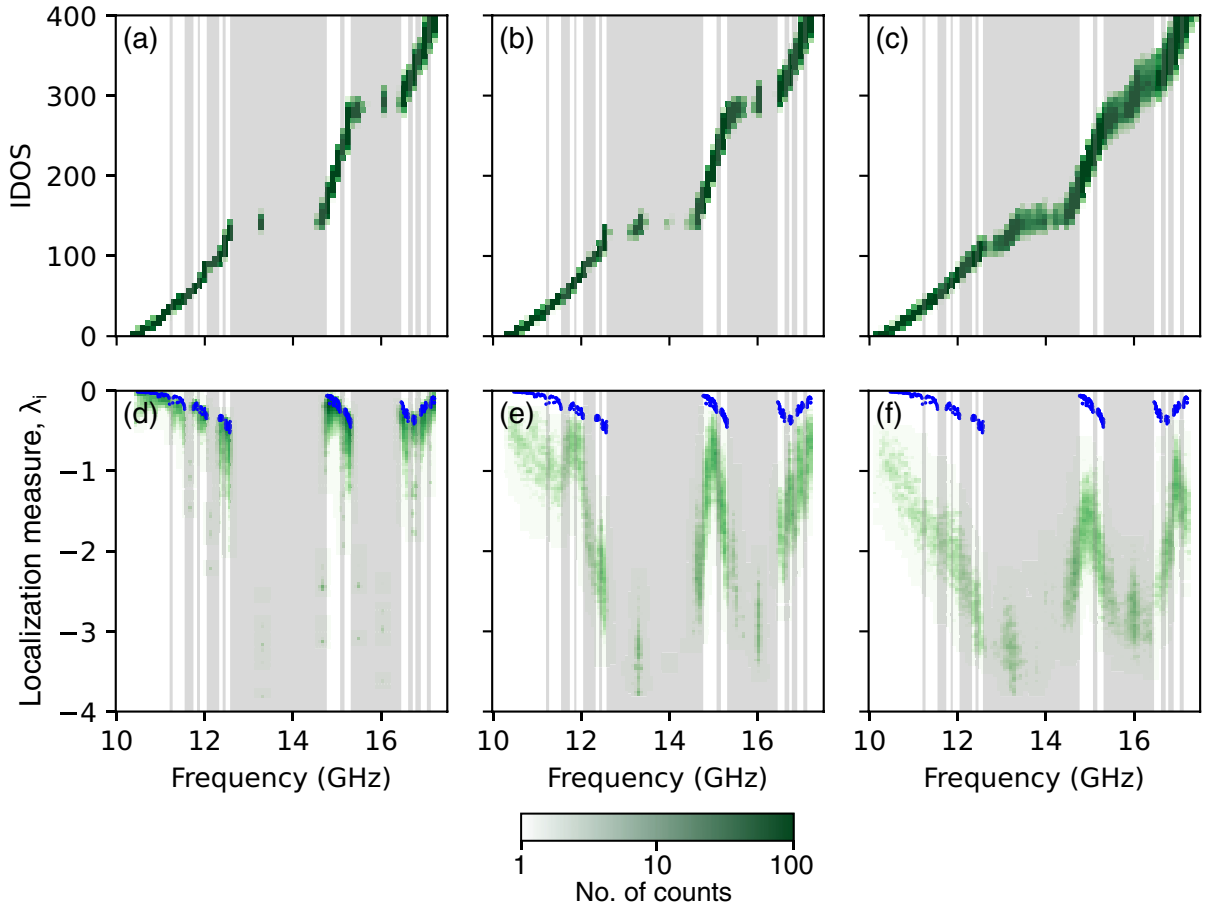

FIG. 4. Top row: (a), (b), and (c) Integrated density of states as a function of frequency plotted in the inverse form f(IDOS) calculated for the Fibonacci sequence with introduced defects. Gray areas represents the frequency gaps in an ideal Fibonacci sequence. The amplitude of phasonic defects $\Delta\phi/(2\pi)$ are (a) 5%, (b) 10%, and (c) 25%. A histogram of integrated density of states (IDOS) is obtained from 100 configurations of differently introduced defects. Intensity of the green color reflects how often a given position is occupied by an SW mode. Bottom row: (d), (e), and (f) Localization measure λ_i as a function of frequency for an SW in a 1D Fibonacci sequence with phasonic defects. The values of λ_i are calculated for structures with (d) 5%, (e) 10%, and (f) 25% of defects. Every plot aggregates 100 different system configurations. λ_i increases significantly even if a small amount of defects is introduced (d), and consequently increases with amount of defects (e) and (f).

narrowest gaps are closed, and new modes strongly localized at defects (see the discussion later in the paper) are induced [see the red dashed frames in Figs. 3(b) and 3(c), showing the states within the frequency gaps]. The narrower gaps are much more susceptible to disappearing with increasing disorder.

In the bottom row of Figs. 3(d)–3(f) we present a Fourier spectra of the structures considered in Figs. 3(a)–3(c). Formation of the frequency gaps can be attributed to the fulfillment of the Bragg condition, i.e., the position of the Bragg peak (multiplied by two) determines the position of frequency gaps [55]. However, their intensity does not necessarily determine the width of the frequency gap. We can see in the unperturbed Fibonacci structure [see Figs. 3(a) and 3(d)] that the biggest peak (except for a peak at $k = 0$) is responsible for the widest frequency gap (12.3–14.3 GHz), however the second biggest peak opens only a small one, around 15 GHz. We can see that the Bragg peaks are reduced as the level of phasonic defect increases. The relative reduction of the highest peaks (corresponding to wider gaps) is smaller than for lower peaks (corresponding to narrower gaps). Therefore, only the highest peaks in the Fourier spectrum are distinguishable, and the widest gaps remain opened for a large level of phasonic defects—see the bottom part of Fig. 3(c) and the zoomed region, marked by the red dashed frame. Another effect of the phasonic defects in IDOS is the change of the slope of f(IDOS) at the edges of frequency gaps. This means that density of states is not singular anymore at these points.

Figures 3(a)–3(c) show that the f(IDOS) is a useful function for description of the spectral properties of defected quasicrystals. However, the spectra presented in Figs. 3(b) and 3(c) are specific for a given, randomly generated, set of phasonic defects. To obtain the representative picture, we need to collect the spectra for many configurations of phasonic defects generated for the same amplitude $\Delta\phi$. Figures 4(a)–4(c) present the IDOS for 100 different configurations aggregated on one plot in the form of a 2D histogram. Please note that figures in two rows of Fig. 4 share the same values of frequency on the horizontal axis. The intensity of the green color reflects which position in frequency and IDOS appear more often. Figures 4(a)–4(c) are plotted for $\Delta\phi/(2\pi) =$

5%, 10%, and 25%, respectively. The gray background marks the frequency gaps of the nondefected Fibonacci sequence. The general trend of IDOS in the function of frequency prevails even for the most disturbed system. The IDOS curve is not much dispersed, suggesting the same spectra for the different realizations of the disorder. However, we can notice that the green line in Fig. 4(c) is thicker than in Fig. 4(a), which indicates some frequency shift under strong disorder. In the range of frequency 10–12 GHz, where IDOS resembles the dispersion relation of the homogeneous film with weight averaged material parameters [black line in Figs. 3(a)–3(c)], defects do not change the picture. The impact of the defects is strongest around the frequency gaps. Initially, for $\Delta\phi/(2\pi) = 5\%$ the modes appear deeply inside and at the edges of the gaps. Then, for higher $\Delta\phi$, the modes start occupying other frequencies within the gaps and gradually fill them. These effects are more effective for narrower gaps. Finally, we do not observe the fine structure of the gaps in the spectrum which was a hallmark of quasiperiodicity. The location of the defect in the sequence and its neighborhood determines the frequency of strongly localized defect modes. For $\Delta\phi/(2\pi) = 5\%$ [Fig. 4(a)] modes from the widest frequency gaps (i.e., the gap around 13 or 16 GHz) are induced by those phasonic defects which form the sequence of double Py strips. Thus, their position on IDOS is very specific. Moreover, since such sequence of strips is common in the defected sequence, the modes are highly degenerated. For a more distorted sequence presented in Figs. 4(b) and 4(c), different sequences become available like triple Py strips, so defect states can occupy other frequencies.

The qualitative determination of localization is challenging because the profiles of the SW modes can be localized in many regions, so the rate of spatial decay cannot be determined unambiguously. Therefore, we decided to introduce the global measure of localization λ_i that is calculated for each ith SW mode $\boldsymbol{m}_i(x)$:

$$\lambda_i = -\frac{1}{L}\int_0^L |m_{i,\mathrm{out}}(x)| \log |m_{i,\mathrm{out}}(x)| dx, \tag{4}$$

where L denotes the width of the whole sequence. For computational simplicity we considered only the out-of-plane component $m_{i,\mathrm{out}}(x)$ of the dynamic part of magnetization $\boldsymbol{m}_i(x)$. During the calculations, the profiles are normalized: $\frac{1}{L}\int_0^L |m_{i,\mathrm{out}}(x)| dx = 1$. The formulation of this measure is done with the analogy to the Shannon information entropy [56,57], where the SW profile plays a role of probability distribution—the uniform distribution (and Dirac delta distribution) corresponds to the highest entropy and complete absence of localization: $\lambda_i = 0$ (the lowest entropy and maximum localization: $\lambda_i = -\infty$).

In Figs. 4(d)–4(f) we present the localization measure λ_i for successive modes, calculated on the same data set as IDOS calculation. They are ordered with increasing frequency, similarly to the IDOS spectrum. We can see that localization is significantly enhanced as the amplitude of the phasonic defects is increasing [green 2D histogram in Figs. 4(d)–4(f)], especially if we compare it to the case of the nondefected system [blue points in Figs. 4(d)–4(f)]. We can identify the strongly localized defect modes with a large value of $|\lambda_i|$

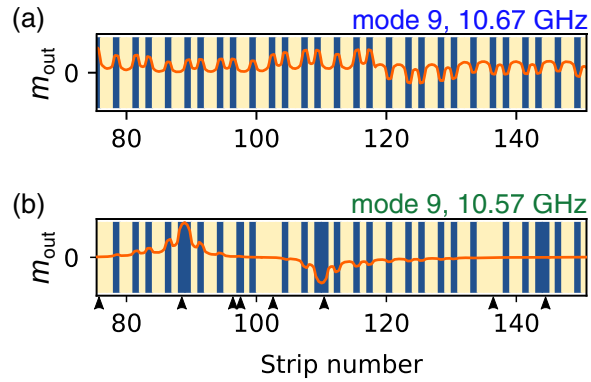

FIG. 5. The evolution of the bulk mode under the presence of the defects. (a) In the absence of defects the mode is not localized, its amplitude is more concentrated in Py than in Co. (b) For $\Delta\phi/(2\pi) = 10\%$ the defects (marked by arrows below the plot) lead to the formation of double Py strips and can concentrate the SW dynamics.

inside the frequency gap. It is worth noting that the localization of the modes at frequencies close to the edges of gaps with enhanced λ_i suggests that some of the critically localized modes [58–61] become defect modes. To inspect the localization of the SW modes directly, we plotted the profiles of selected modes. We chose one of the configurations for $\Delta\phi = 10\%$ that corresponds to an intermediate disorder level, presented in Figs. 4(b) and 4(e). All the modes are normalized to the maximum absolute value in the whole structure. Figures present only fragments of them, and the location can be deduced from strip numbers. All modes, which were selected for plotting, are also marked in the spectra [Figs. 3(a) and 3(c)]. We start the analysis by checking the impact of the disorder on the bulk modes. Figure 5 presents the comparison of one mode, labeled No. 9 at 10.67 and 10.57 GHz in nondefected and defected structures, respectively. Looking at Fig. 4(e) suggests significant modification of the profile. The envelope in Fig. 5(a) is not localized and the mode has several nodal points (one of them is visible close to strip No. 120). The visible nonuniformity of amplitude is related to the oscillatory and evanescent behavior in Py and Co strips, respectively, thus SW amplitude is concentrated in Py strips. Figure 5(b) presents mode No. 9 after introducing the defects, where double Py strips are formed. SW is localized on the defects, around the strips No. 90 and No. 110 that have a similar local arrangement.

In nondefected Fibonacci quasicrystals, the critically localized modes exist close to the edges of the gaps—see mode No. 136 at 12.57 GHz in Fig. 6(a) and its frequency marked in Fig. 3(c). The profile of this mode exhibits the pattern with amplitude concentrated on parts of the structure possessing locally the same arrangement of strips. For very large structures, these modes can reveal a self-similar pattern [58,61]. By adding the defects, we can shift critically localized modes to the frequency gap. Then, their frequencies are changed significantly, and the profiles are extremely strongly localized at defects, see Fig. 6(b). The SW in Fig. 6(b) is localized in double Py, and since such defects occur several times within

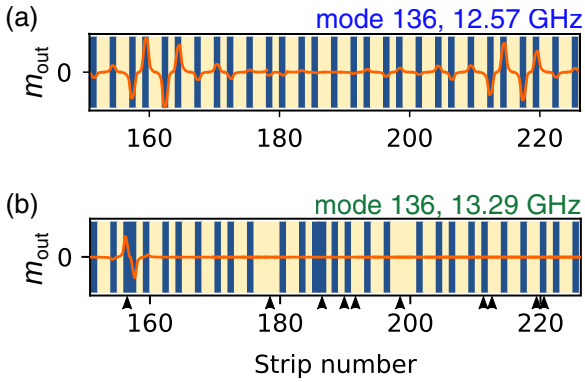

FIG. 6. The transition of the mode No. 136 from critically localized at the edge of the frequency gap to strongly localized in the frequency gap induced by phasonic defects. The critically localized mode (a) enters into the gap and (b) becomes strongly localized, due to the presence of defects $\Delta\phi/(2\pi) = 10\%$ which is accompanied by a significant change in frequency from 12.57 to 13.29 GHz.

the considered structure, the mode can occupy different defects leading to multiple degenerations.

The bulk modes can also increase their localization due to partial confinement between the defects. Figure 7(a) presents the critically localized mode No. 359 at 16.96 GHz, which has an enhanced amplitude on the sequences Co|Co|Py|Co (or on their reversed copies Co|Py|Co|Co). After introducing the defects, the mode amplitude is redistributed among these strips, which leads to the partial confinement of this mode between the defects, see Fig. 7(b).

The most typical kind of localization, existing in both periodic and quasiperiodic structures, is an exponential localization on defects, which are observed within the frequency gaps. We selected two wide gaps, around the frequency 13.5 or 16 GHz (Figs. 3 and 4), to investigate the profiles of defect modes. The selected modes (shown in Fig. 8) are localized at the defects, which have the form of double Py strips. We arbitrary chose the modes with one phase flip inside the single defect [Figs. 8(a) and 8(b)], and three phase's flips inside the defect [Figs. 8(c) and 8(d)]. The defect modes are located at a single or few positions in the structure. Due to strong localization and low probability of overlapping between the profiles concentrated at selected defects, the modes are degenerated—there are many modes of very similar frequencies occupying similar sequences in different locations of the quasicrystal. We discussed earlier the position-dependent susceptibility for inducing the defects, where we showed that some locations in the structure are very resistant or even completely robust to the introduction of defects at the low value of the amplitude $\Delta\phi$ [35]. This is an additional factor supporting the isolation of the SW dynamics at defects and contributing to the nonuniform distribution of the frequencies for defect modes within the frequency gaps.

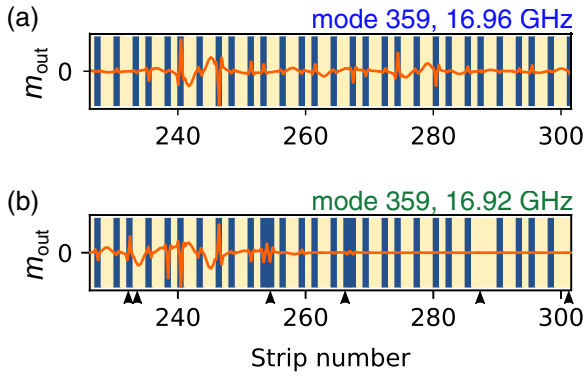

FIG. 7. (a) The critically localized mode (No. 359 at 16.96 GHz) which increases its localization and slightly changes its frequency to $f = 16.92$ GHz due to partial confinement between defects (b) at $\Delta\phi/(2\pi) = 10\%$.

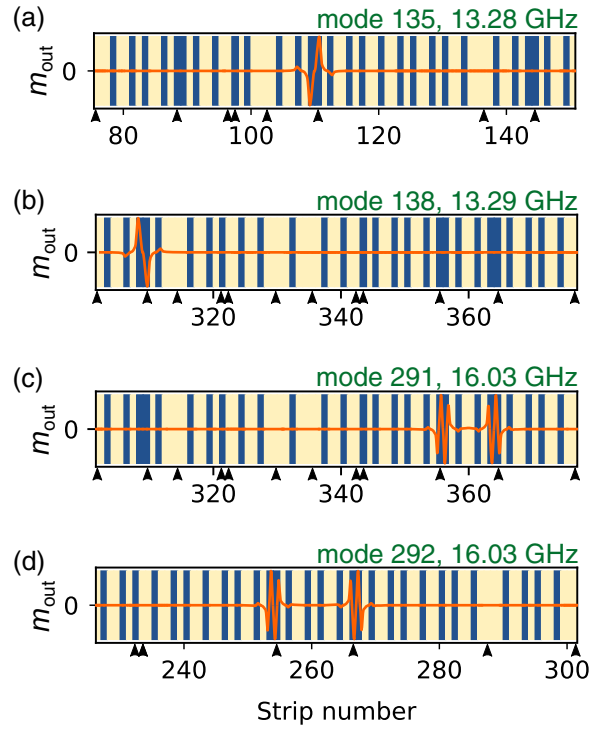

FIG. 8. The defect modes from the two largest frequency gaps shown in Figs. 3 and 4. (a) and (b) Modes No. 135 and No. 138 with frequency 13.28 and 13.29 GHz. (c) and (d) Modes No. 291 and No. 292 with frequency 16.03 GHz. The modes are strongly localized at one of few locations but have the same profile, differing only in phase (flipped upside down) [see (a) and (b)] or reversed along with the structure (flipped left-right) [see (c) and (d)]. Due to strong localization, the modes are practically degenerated. The results are shown for the structure with $\Delta\phi/(2\pi) = 10\%$.

IV. SUMMARY

It is known that magnonic quasicrystals offer additional possibilities in designing artificial magnonic band structures as compared to magnonic crystals. The increased complexity of the spin-wave spectrum and the appearance of bulk localization of the spin-wave modes are the main effects of the quasiperiodicity. In the paper we show additional steps towards customization, namely the introduction of the disorder in the form of phasonic defects, and demonstrate their impact on spectral properties and localization of the spin-wave modes. To explore the role of disorder in quasicrystals, we

studied many randomly generated configurations of defects. We focused on selected configurations to discuss the profiles of representative eigenmodes exhibiting the critical localization at the edges of the frequency gaps, and strong localization on phasonic defects inside the gaps. In particular, we show that smaller gaps are closed under a small perturbation of the quasiperiodicity, while wide ones are relatively robust to a disorder. It is assisted by transition from bulk modes to critically localized modes, and finally to the modes strongly localized on the defects. Interestingly, the modes from the frequency gap edges become strongly localized by the introduction of phasonic defects to the structure, which is correlated with the disappearance of van Hove singularities.

We demonstrated that in the complex magnonic system, where both short-range exchange interactions and long-range dipolar interactions come into play, the effects like closing the small gaps and enhancement of the modes' localization are reproduced for spin waves. The study opens the route for the investigation of phasonic defects in two-dimensional magnonic quasicrystals, which recently attracted interest due to their application potential in magnonics signal processing [49,62].

ACKNOWLEDGMENTS

S.M. and J.W.K. would like to thank Radosław Strzałka for fruitful discussion. All authors would like to acknowledge the financial support from the National Science Centre, Poland (Projects: No. 2020/36/T/ST3/00542, No. 2020/37/B/ST3/03936, and No. 2020/39/O/ST5/02110).

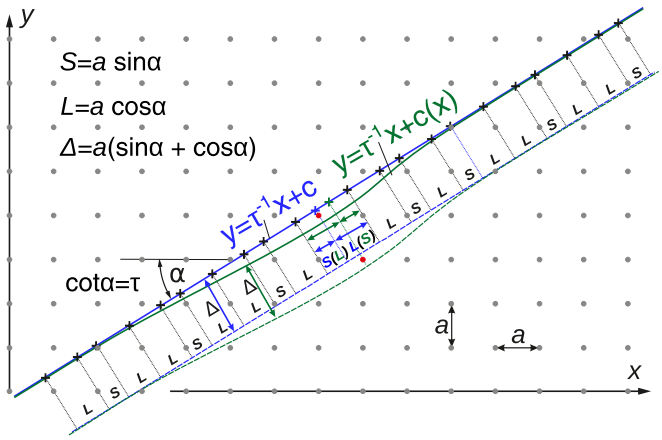

FIG. 9. The illustration of the cut-and-projection (C&P) method and the induction of phasonic defect. The array of dots represent the square lattice in a 2D hyperspace. The Fibonacci lattice (black and blue crosses) is generated by the projection of a square lattice from the belt between solid and dashed lines onto the line $y = \tau^{-1}x + c$ of irrational slope, being the inverse of the golden ratio τ. The visible (21-element) section of the Fibonacci lattice corresponds to the selection of $\phi = 2\pi c/a = 0.8$, see Fig. 1. For a defect-free Fibonacci lattice the belt (between solid blue and dashed blue line) is straight. By bending the belt (limited here by solid green and dashed green lines), we can induce the phasonic defects in the Fibonacci lattice (black and green crosses).

APPENDIX A: CUT-AND-PROJECT METHOD: PHASONS

The Fibonacci lattice can be generated from the square lattice of the period a by the C&P method [3]. The lattice points $\mathbf{r} = a(m\hat{\mathbf{x}} + n\hat{\mathbf{y}})$, where m, n are integers, are projected onto the line $y = \tau^{-1}x + c$ from the belt, below this line, of the width $a(\cos\alpha + \sin\alpha) = a(\tau + 1)/\sqrt{\tau + 2}$, where $\alpha = \mathrm{arccot}(\tau)$ is the angle between the line and the x direction, and τ is the golden ratio. This procedure generates the proper sequence of long ($L = a\cos\alpha = a\tau/\sqrt{\tau + 2}$) and short distances ($S = a\sin\alpha = a/\sqrt{\tau + 2}$) between lattice points projected onto the line y, forming the Fibonacci lattice, see Fig. 9. The position of the line (given by the constant c) and the related shift in the perpendicular direction $\sqrt{\tau + 2}(-\hat{\mathbf{x}} + \tau\hat{\mathbf{y}})$ express the structural degree of freedom in defining a Fibonacci lattice. Regardless, on the value of this shift, we always obtain the defectless lattices, differing only in some uniform translation of the lattice sites along the real (parallel) direction $\sqrt{\tau + 2}(\tau\hat{\mathbf{x}} + \hat{\mathbf{y}})$.

The introduction of phasonic defect can be described by bending the belt. It is equivalent to the perturbation of structural degree of freedom, which can be expressed here as a position-dependent shift of the belt: $c(x)$. When this dependence is small and smooth at the distances larger than the lattice constant a, then the phasonic defects have a form of

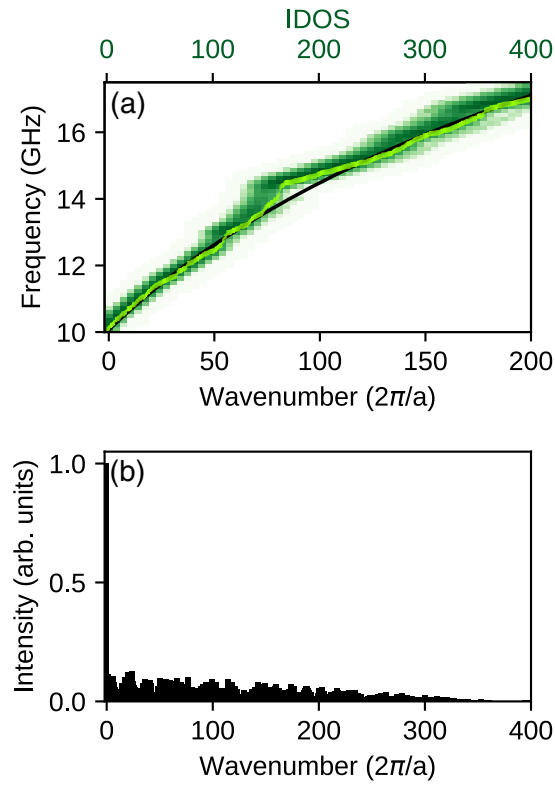

FIG. 10. (a) Integrated density of states for SWs in the randomly generated sequence of Co and Py, where the ratio between types of strips is kept as for a Fibonacci quasicrystal, i.e., it corresponds to the golden ratio. The dark-green color represents a histogram of aggregated results obtained from 100 different random sequences (the color scale is the same as in Fig. 4). Light-green points stand for one specific structure for which the bar of the Fourier transform (b) are plotted.

the swaps between neighboring short and long distances in the Fibonacci lattice ($S \leftrightarrow L$).

APPENDIX B: RANDOM SYSTEM

In Fig. 10(a) we show the IDOS spectrum of the SW eigenmodes in a randomized sequence of Co and Py with the same parameter as in the paper. To keep the same averaged composition, we used 144 Py and 233 Co strips. We generated 100 different configurations, and the intensity of the green color reflects how often a specific position is occupied on the plot. By light green we plotted one selected configuration, for which Fourier spectrum is presented below. The IDOS spectrum of this exemplary configuration coincides with the SW dispersion relation for a uniform ferromagnetic layer with the volume averaged material parameters (i.e., with the weights $1/\tau$ and $1 - 1/\tau$), except for a small deviation around 14 GHz. The IDOS does not show any signatures of the frequency gaps. It is also reflected in the Fourier spectrum [Fig. 10(b)] of this random structure that do not have any distinctive peaks except the peak at wave number $k = 0$, which corresponds to the average value of the spatial distribution of material parameters. The absence of Bragg peaks is the signature of the lack of (quasi)crystal long-range order.

The introduction of a phasonic defect for large approximates of the Fibonacci quasicrystal does not change the average number of Co and Py strips (it is obvious for the swaps Co $\leftrightarrow$ Py, whereas the substitutions Co $\rightarrow$ Py and Py $\rightarrow$ Co are equally probable, see Fig. 1). In the limit $\Delta\phi \rightarrow 2\pi$ the IDOS spectrum approaches the spectrum of the disordered system, as shown in Fig. 10(a).

[1] D. Shechtman, I. Blech, D. Gratias, and J. W. Cahn, Metallic Phase with Long-Range Orientational Order and No Translational Symmetry, Phys. Rev. Lett. **53**, 1951 (1984).

[2] D. Levine and P. J. Steinhardt, Quasicrystals: A New Class of Ordered Structures, Phys. Rev. Lett. **53**, 2477 (1984).

[3] C. Janot, *Quasicrystals: A Primer* (Oxford University Press, Oxford, 2012).

[4] Z. V. Vardeny, A. Nahata, and A. Agrawal, Optics of photonic quasicrystals, Nat. Photonics **7**, 177 (2013).

[5] L. Dal Negro, *Optics in Aperiodic Structures: Fundamentals and Device Applications* (CRC, Boca Raton, FL, 2014).

[6] T. Janssen, G. Chapuis, and M. De Boissieu, *Aperiodic Crystals From Modulated Phases to Quasicrystalss* (Oxford University Press, Oxford, 2007).

[7] P. W. Anderson, Absence of diffusion in certain random lattices, Phys. Rev. **109**, 1492 (1958).

[8] L. Levi, M. Rechtsman, B. Freedman, T. Schwartz, O. Manela, and M. Segev, Disorder-enhanced transport in photonic quasicrystals, Science **332**, 1541 (2011).

[9] M. Segev, Y. Silberberg, and D. N. Christodoulides, Anderson localization of light, Nat. Photonics **7**, 197 (2013).

[10] J. A. Kromer, M. Schmiedeberg, J. Roth, and H. Stark, What Phasons Look Like: Particle Trajectories in a Quasicrystalline Potential, Phys. Rev. Lett. **108**, 218301 (2012).

[11] A. Jagannathan, The Fibonacci quasicrystal: Case study of hidden dimensions and multifractality, Rev. Mod. Phys. **93**, 045001 (2021).

[12] E. Maciá, The role of aperiodic order in science and technology, Rep. Prog. Phys. **69**, 397 (2006).

[13] J. E. S. Socolar, T. C. Lubensky, and P. J. Steinhardt, Phonons, phasons, and dislocations in quasicrystals, Phys. Rev. B **34**, 3345 (1986).

[14] M. de Boissieu, Phonons, phasons and atomic dynamics in quasicrystals, Chem. Soc. Rev. **41**, 6778 (2012).

[15] J. Wolny, I. Buganski, and R. Strzalka, Phononic and phasonic Debye-Waller factors for 1D quasicrystals, Acta Phys. Pol. A **130**, 836 (2016).

[16] B. Freedman, R. Lifshitz, J. W. Fleischer, and M. Segev, Phason dynamics in nonlinear photonic quasicrystals, Nat. Mater. **6**, 776 (2007).

[17] M. A. Bandres, M. C. Rechtsman, and M. Segev, Topological Photonic Quasicrystals: Fractal Topological Spectrum and Protected Transport, Phys. Rev. X **6**, 011016 (2016).

[18] C. H. Chen, R. Z. Qiu, C. H. Chang, and W. J. Hsueh, Strongly localized modes in one-dimensional defect-free magnonic quasicrystals, AIP Adv. **4**, 087102 (2014).

[19] J. Rychły, J. W. Kłos, M. Mruczkiewicz, and M. Krawczyk, Spin waves in one-dimensional bicomponent magnonic quasicrystals, Phys. Rev. B **92**, 054414 (2015).

[20] J. Ding, M. Kostylev, and A. O. Adeyeye, Magnonic Crystal as a Medium with Tunable Disorder on a Periodical Lattice, Phys. Rev. Lett. **107**, 047205 (2011).

[21] M. Evers, C. A. Müller, and U. Nowak, Spin-wave localization in disordered magnets, Phys. Rev. B **92**, 014411 (2015).

[22] M. Evers, C. A. Müller, and U. Nowak, Weak localization of magnons in chiral magnets, Phys. Rev. B **97**, 184423 (2018).

[23] P. Buczek, S. Thomas, A. Marmodoro, N. Buczek, X. Zubizarreta, M. Hoffmann, T. Balashov, W. Wulfhekel, K. Zakeri, and A. Ernst, Spin waves in disordered materials, J. Condens. Matter Phys. **30**, 423001 (2018).

[24] R. A. Gallardo, T. Schneider, A. Roldán-Molina, M. Langer, A. S. Núñez, K. Lenz, J. Lindner, and P. Landeros, Symmetry and localization properties of defect modes in magnonic superlattices, Phys. Rev. B **97**, 174404 (2018).

[25] V. S. Tkachenko, V. V. Kruglyak, and A. N. Kuchko, Spectrum and reflection of spin waves in magnonic crystals with different interface profiles, Phys. Rev. B **81**, 024425 (2010).

[26] V. V. Kruglyak, M. L. Sokolovskii, V. S. Tkachenko, and A. N. Kuchko, Spin-wave spectrum of a magnonic crystal with an isolated defect, J. Appl. Phys. **99**, 08C906 (2006).

[27] H. Yang, G. Yun, and Y. Cao, Point defect states of exchange spin waves in all-ferromagnetic two-dimensional magnonic crystals, J. Appl. Phys. **111**, 013908 (2012).

[28] H. Yang, G. Yun, and Y. Cao, Coupling characteristics of point defects modes in two-dimensional magnonic crystals, J. Appl. Phys. **112**, 103911 (2012).

[29] H. Yang, G. Yun, and Y. Cao, Effects of point defect shapes on defect modes in two-dimensional magnonic crystals, J. Magn. Magn. Mater. **356**, 32 (2014).

[30] D. Xing, H. Yang, and Y. Cao, Waveguide properties in two-dimensional magnonic crystals with line defects, J. Magn. Magn. Mater. **377**, 286 (2015).

[31] K. Baumgaertl, S. Watanabe, and D. Grundler, Phase control of spin waves based on a magnetic defect in a one-dimensional magnonic crystal, Appl. Phys. Lett. **112**, 142405 (2018).

[32] Y. E. Kraus and O. Zilberberg, Topological Equivalence between the Fibonacci Quasicrystal and the Harper Model, Phys. Rev. Lett. **109**, 116404 (2012).

[33] A. Dareau, E. Levy, M. B. Aguilera, R. Bouganne, E. Akkermans, F. Gerbier, and J. Beugnon, Revealing the Topology of Quasicrystals with a Diffraction Experiment, Phys. Rev. Lett. **119**, 215304 (2017).

[34] E. Levy, A. Barak, A. Fisher, and E. Akkermans, Topological properties of Fibonacci quasicrystals: A scattering analysis of Chern numbers, arXiv:1509.04028.

[35] G. G. Naumis, Phason hierarchy and electronic stability of quasicrystals, Phys. Rev. B **71**, 144204 (2005).

[36] Z. K. Wang, V. L. Zhang, H. S. Lim, S. C. Ng, M. H. Kuok, S. Jain, and A. O. Adeyeye, Observation of frequency band gaps in a one-dimensional nanostructured magnonic crystal, Appl. Phys. Lett. **94**, 083112 (2009).

[37] S. Choudhury, S. Saha, R. Mandal, S. Barman, Y. Otani, and A. Barman, Shape- and interface-induced control of spin dynamics of two-dimensional bicomponent magnonic crystals, ACS Appl. Mater. Interfaces **8**, 18339 (2016).

[38] A. Wawro, Z. Kurant, M. Jakubowski, M. Tekielak, A. Pietruczik, R. Böttger, and A. Maziewski, Magnetic Properties of Coupled Co/Mo/Co Structures Tailored by Ion Irradiation, Phys. Rev. Applied **9**, 014029 (2018).

[39] L. Frąckowiak, P. Kuświk, G. D. Chaves-O'Flynn, M. Urbaniak, M. Matczak, P. P. Michałowski, A. Maziewski, M. Reginka, A. Ehresmann, and F. Stobiecki, Magnetic Domains without Domain Walls: A Unique Effect of He^+ Ion Bombardment in Ferrimagnetic Tb/Co Films, Phys. Rev. Lett. **124**, 047203 (2020).

[40] P. Graczyk, M. Krawczyk, S. Dhuey, W.-G. Yang, H. Schmidt, and G. Gubbiotti, Magnonic band gap and mode hybridization in continuous permalloy films induced by vertical dynamic coupling with an array of permalloy ellipses, Phys. Rev. B **98**, 174420 (2018).

[41] C. Liu, J. Chen, F. Heimbach, H. Yu, Y. Xiao, J. Hu, M. Liu, H. Chang, T. Stueckler, S. Tu, Y. Zhang, Y. Zhang, P. Gao, Z. Liao, D. Yu, K. Xia, N. Lei, W. Zhao, and M. Wu, Long-distance propagation of short-wavelength spin waves, Nat. Commun. **9**, 738 (2018).

[42] C. L. Chang, S. Mieszczak, M. Zelent, V. Besse, U. Martens, R. R. Tamming, J. Janusonis, P. Graczyk, M. Münzenberg, J. W. Kłos, and R. I. Tobey, Driving Magnetization Dynamics in an on-Demand Magnonic Crystal via the Magnetoelastic Interactions, Phys. Rev. Applied **10**, 064051 (2018).

[43] R. F. L. Evans, D. Hinzke, U. Atxitia, U. Nowak, R. W. Chantrell, and O. Chubykalo-Fesenko, Stochastic form of the Landau-Lifshitz-Bloch equation, Phys. Rev. B **85**, 014433 (2012).

[44] M. Krawczyk, M. L. Sokolovskyy, J. W. Kłos, and S. Mamica, On the formulation of the exchange field in the Landau-Lifshitz equation for spin-wave calculation in magnonic crystals, Adv. Condens. Matter Phys. **2012**, 764783 (2012).

[45] J. W. Kłos, M. Krawczyk, and M. Sokolovskyy, Bulk and edge modes in two-dimensional magnonic crystal slab, J. Appl. Phys. **109**, 07D311 (2011).

[46] S. Mieszczak and J. W. Kłos, Interface modes in planar one-dimensional magnonic crystals, Sci. Rep. **12**, 11335 (2022).

[47] S. Pan, J. W. Kłos, S. Mieszczak, A. Barman, and M. Krawczyk, Spin waves in periodic antidot waveguide of complex base, J. Phys. D **50**, 275003 (2017).

[48] J. Rychły, S. Mieszczak, and J. Kłos, Spin waves in planar quasicrystal of penrose tiling, J. Magn. Magn. Mater. **450**, 18 (2018).

[49] S. Watanabe, V. S. Bhat, K. Baumgaertl, and D. Grundler, Direct observation of worm-like nanochannels and emergent magnon motifs in artificial ferromagnetic quasicrystals, Adv. Funct. Mater. **30**, 2001388 (2020).

[50] P. Vignolo, M. Bellec, J. Böhm, A. Camara, J.-M. Gambaudo, U. Kuhl, and F. Mortessagne, Energy landscape in a penrose tiling, Phys. Rev. B **93**, 075141 (2016).

[51] L. van Hove, The occurrence of singularities in the elastic frequency distribution of a crystal, Phys. Rev. **89**, 1189 (1953).

[52] N. W. Ashcroft and D. N. Mermin, *Solid State Physics* (Harcourt College Publishers, San Diego, CA, 1976).

[53] F. Lisiecki, J. Rychły, P. Kuświk, H. Głowiński, J. W. Kłos, F. Groß, I. Bykova, M. Weigand, M. Zelent, E. J. Goering, G. Schütz, G. Gubbiotti, M. Krawczyk, F. Stobiecki, J. Dubowik, and J. Gräfe, Reprogrammability and Scalability of Magnonic Fibonacci Quasicrystals, Phys. Rev. Applied **11**, 054003 (2019).

[54] B. A. Kalinikos and A. N. Slavin, Theory of dipole-exchange spin wave spectrum for ferromagnetic films with mixed exchange boundary conditions, J. Phys.: Condens. Matter **19**, 7013 (1986).

[55] M. E. Limonov and R. E. De La Rue, *Optical Properties of Photonic Structures* (CRC, Boca Raton, FL, 2012).

[56] B. Mirbach and H. J. Korsch, Phase Space Entropy and Global Phase Space Structures of (Chaotic) Quantum Systems, Phys. Rev. Lett. **75**, 362 (1995).

[57] B. Mirbach and H. J. Korsch, A generalized entropy measuring quantum localization, Ann. Phys. **265**, 80 (1998).

[58] M. Kohmoto, B. Sutherland, and C. Tang, Critical wave functions and a cantor-set spectrum of a one-dimensional quasicrystal model, Phys. Rev. B **35**, 1020 (1987).

[59] E. Maciá and F. Domínguez-Adame, Physical Nature of Critical Wave Functions in Fibonacci Systems, Phys. Rev. Lett. **76**, 2957 (1996).

[60] L. Dal Negro, C. J. Oton, Z. Gaburro, L. Pavesi, P. Johnson, A. Lagendijk, R. Righini, M. Colocci, and D. S. Wiersma, Light Transport through the Band-Edge States of Fibonacci Quasicrystals, Phys. Rev. Lett. **90**, 055501 (2003).

[61] H. Aynaou, A. Mouadili, N. Ouchani, E. H. El Boudouti, A. Akjouj, and B. Djafari-Rouhani, Scaling law, confined and surface modes in photonic Fibonacci stub structures: Theory and experiment, Appl. Sci. **10**, 7767 (2020).

[62] S. Watanabe, V. S. Bhat, K. Baumgaertl, M. Hamdi, and D. Grundler, Direct observation of multiband transport in magnonic penrose quasicrystals via broadband and phase-resolved spectroscopy, Sci. Adv. **7**, eabg3771 (2021).